HHS Public Access

Author manuscript

Nat Struct Mol Biol. Author manuscript; available in PMC 2019 December 24.

Published in final edited form as:

Nat Struct Mol Biol. 2019 July ; 26(7): 599–606. doi:10.1038/s41594-019-0245-7.

Structures of human ENT1 in complex with adenosine reuptake inhibitors

Nicholas J. Wright[1], **Seok-Yong Lee**[1,†]

[1]Department of Biochemistry, Duke University Medical Center, 303 Research Drive, Durham, North Carolina, 27710, USA

Abstract

The human Equilibrative Nucleoside Transporter 1 (hENT1), a member of the SLC29 family, plays crucial roles in adenosine signaling, cellular uptake of nucleoside for DNA and RNA synthesis, and nucleoside-derived anticancer and antiviral drug transport in human. Because of its central role in adenosine signaling, it is the target of adenosine reuptake inhibitors (AdoRI), several of which are clinically used. Despite its importance in human physiology and pharmacology, the molecular basis of hENT1-mediated adenosine transport and its inhibition by AdoRIs are limited due to the absence of structural information on hENT1. Here we present crystal structures of hENT1 in complex with two chemically distinct AdoRIs: dilazep and *S*-(4-Nitrobenzyl)-6-thioinosine (NBMPR). Combined with mutagenesis study, our structural analyses elucidate two distinct inhibitory mechanisms exhibited on hENT1, while giving insight into adenosine recognition and transport. Our studies provide the platform for improved pharmacological intervention of adenosine and nucleoside analog drug transport by hENT1.

Equilibrative Nucleoside Transporters (ENTs), members of the solute carrier transporter family SLC29, are integral membrane proteins that play central roles in nucleoside-related physiology, pathophysiology, and pharmacology[1,2]. There are four human ENT isoforms (hENT1-hENT4), each of which exhibit diverse tissue and subcellular localizations, substrate specificities and pharmacological properties. Of these, hENT1 has been the central focus of many studies owing to its crucial role in adenosine and nucleoside analog drug transport[1–4].

Adenosine is a key signaling molecule affecting cardiovascular function and neuromodulation in the human physiological and pathological states including epilepsy, alcohol preference, pain, ischemia, and inflammation[5–7]. hENT1, an energy-independent uniporter with a preferred specificity for adenosine, is responsible for controlling adenosine signaling by regulating its extracellular and intracellular levels, and thus is the target of adenosine reuptake inhibitors (AdoRIs)[1,2,8,9]. A chemically diverse group of nucleoside-

†Correspondence to: S.-Y. Lee. seok-yong.lee@duke.edu, tel: 919-684-1005, fax: 919-684-8885.

Author Contributions N.J.W. solved the structures and performed all experiments under the guidance of S.-Y.L. N.J.W. and S.-Y.L. wrote the paper.

Competing Interests Statement: The authors declare no competing financial interests.

analogues and non-nucleosides, AdoRIs increase extracellular concentration of adenosine by blocking hENT1 function and are clinically used as vasodilators and antithrombotic drugs for the treatment of cardiopathy, renal disorders, and hypertension[1,2,10,11]. There has been recent interest in improving the pharmacological properties of AdoRIs, along with the identification of novel human ENT1 inhibitors[12–15].

hENTs are responsible for the transport of over 30 Food and Drug Administration (FDA) or European Medicines Agency (EMA) approved nucleoside-derived anticancer, antiviral, and antihypertensive drugs[2]. Importance of hENT1 for the efficacies of these drugs is highlighted by numerous studies which report a high level of correlation between hENT1 expression and survival outcome of pancreatic cancer patients treated with the nucleoside-derived anticancer agent gemcitabine[16–23].

Despite the importance of hENT1, our understanding of hENT1 and its inhibition by AdoRIs is limited, partly due to the fact no experimental structure is available for any SLC29 family transporter[1]. Further, the SLC29 family is evolutionarily distinct from the structurally characterized SLC28 concentrative nucleoside transporter family[24–26]. Additionally, the ENT family does not have any prokaryotic orthologs and AdoRI action is highly isoform and species-specific[1,2], requiring structural study of hENT1 in complex with AdoRIs to understand the mechanism of inhibition exhibited on the transporter. Here we present two structures of hENT1: one in complex with the adenosine analog AdoRI *S*-(4-Nitrobenzyl)-6-thioinosine (NBMPR) and the other in complex with the non-nucleoside AdoRI dilazep, a clinically used vasodilator. To our knowledge, these are the first experimental structures to describe the SLC29 family protein fold. Together with functional studies, the structural data presented here provides mechanistic insights into hENT1-mediated adenosine transport and its inhibition. Notably, we found that NBMPR blocks the transporter in a unique manner, which provides mechanistic insights into the inner workings of hENT1 and a starting point for the rational design of therapeutics with enhanced pharmacological properties.

Crystallization of human ENT1 in complex with dilazep or NBMPR

To achieve a level of stability required for structural study, point mutations and disordered-loop truncations were screened for enhanced biochemical behavior (see Methods). After exhaustive screening, three point mutations (Leu168Phe, Pro175Ala and Asn288Lys) were identified to enhance transporter detergent solution behavior. Additionally, a disordered loop truncation (ΔPro243-Gln274) previously reported to have no effect on hENT1 functional activity[27] was found to greatly enhance detergent solution behavior of the transporter. Combining this loop truncation and three point mutations resulted in a functionally competent construct ($hENT1_{cryst}$, Supplementary Note 1) which mediates nucleoside transport to a level consistent with a previous report[28] (Supplementary Fig. 1), while retaining binding capacity to the human ENT1-specific inhibitor NBMPR (Fig. 1a). The transporter behavior was further enhanced substantially by incorporating the non-nucleoside AdoRI dilazep during protein expression and purification. The dilazep-bound $hENT1_{cryst}$ was crystallized in lipidic cubic phase, yielding diffraction of X-rays to 2.3 Å resolution. Experimental phases to 3.5 Å were obtained by single-isomorphous replacement anomalous

scattering (SIRAS) from platinum-soaked crystals (Table 1 and Supplementary Fig. 2). The final dilazep-bound human ENT1 structure is of excellent quality with a Free-R factor of 24%. We also crystallized $hENT1_{cryst}$ in complex with the nucleoside-derived AdoRI NBMPR, which exhibits merohedral twinning. Phases were obtained from the dilazep-bound hENT1 structure by molecular replacement, and refinement was carried out against the X-ray data to 2.9 Å resolution (see Methods) (Figure 1b and Supplementary Fig. 3).

Transporter architecture

Dilazep-bound $hENT1_{cryst}$ was crystallized as a single monomer in the asymmetric unit. Consistent with previous accessibility studies of hENT1[29], $hENT1_{cryst}$ is composed of 11-transmembrane (TM) helices with the N-terminus in the cytosolic side and the C-terminus in the extracellular side (Fig. 1c–d). The structural architecture of the transporter exhibits a pseudo-symmetric 6+5 topology in which the first 6 TM forms one bundle which we termed the N-domain, and the final 5 TMs forms another bundle in which we term the C-domain (Fig. 1c–d, Supplementary Fig. 4a). It was previously speculated that the fold of ENT bears similarity to that of Major Facilitator Superfamily (MFS) transporters, which exhibit a 6+6 topology and pseudo-symmetry between the first 6 TMs in the N-domain and the second 6 TMs in the C-domain[1,2]. Structural superposition of $hENT1_{cryst}$ to human Glut3[30], a representative outward-facing MFS X-ray structure, shows that despite the low sequence identity (~17% sequence identity) and structural similarity (Cα R.M.S.D. of 5.0 Å), the fold of hENT1 matches the first 11 TMs (TM1-TM11) out of 12 TMs in MFS (Supplementary Fig. 4b). Several structural features observed in $hENT1_{cryst}$ are distinct from features consistent within MFS. First, because TM12 is absent in hENT1, TM9 in hENT1 is arranged to fit in to the space that is occupied by both TM9 and TM12 in MFS, and thus the location of TM9 in hENT1 is substantially different from TM9 in canonical MFS transporters. (Supplementary Fig. 4b). Second, because of the asymmetry in the composition between the N- and the C-domains in hENT1, the structural symmetry in the two domains is relatively lower with a Cα R.M.S.D. of 4.0 Å, compared to that of 3.0 Å in the canonical MFS transporter LacY or 3.3 Å in the MFS transporter hGlut3[30,31].

The AdoRIs NBMPR and dilazep occupy the central cavity of the transporter, accessible to the extracellular side of the membrane, suggesting that both structures represent outward-facing conformations, consistent with the predictions from previous functional studies (Fig. 2a)[32–35]. In both inhibitor-bound structures, the narrowest constriction point at the extracellular side occurs between Met33 of TM1 and Pro308 of TM7. Following the nomenclatures of MFS and SLC transporters, we tentatively assign this region as the “extracellular thin gate”. The surface representations suggest that the thin gate prevents NBMPR from releasing into the extracellular side freely in the NBMPR-bound hENT1 structure, thus representing an outward-facing occluded conformation. On the contrary, a substantial part of dilazep is cradled around the thin gate, preventing complete occlusion of the thin gate (Fig. 2a and 2b). At the cytosolic-facing side of $hENT1_{cryst}$, TM4, TM5, TM10 and TM11 feature extensive hydrophobic contacts, fully occluding access from the cytosolic side. Additional polar and charged interactions appear to stabilize this cytosolic gate of $hENT1_{cryst}$ (Fig. 2b). We propose that this extensive network of hydrophobic, polar and charged interactions form the intracellular thick gate. Of these polar and charged

interactions, Arg111 and Glu428 are exclusively conserved across mammalian ENTs, as well as highly conserved across the entire ENT family, suggesting a functional role for these residues (Fig. 2b). Further, this interaction network observed between the two symmetry related halves of $hENT1_{cryst}$ at this site is distinct from the highly-conserved A-motif of MFS[36], which is located at a structurally conserved position in human Glut3, suggesting a difference in transport mechanisms between the SLC29 family and MFS (Supplementary Fig. 4c).

Dilazep binding site

A strong and unambiguous electron density peak for dilazep was observed early in model refinement against the high-resolution native data (Fig. 3a and Supplementary Fig. 2). Dilazep, comprised of two trimethoxybenzoic acid groups linked to a diazepane ring in the middle, adopts a crescent conformation. Each of the trimethoxyphenyl rings occupies a distinct site: one site deep within the central cavity, and the other proximal to the extracellular side. Mapping previous mutagenesis studies indicate that amino acid residues important for nucleoside recognition are located in the central cavity[37–41] (Supplementary Fig. 5a). We therefore term the site within the central cavity “orthosteric site” and the other site near the extracellular side “opportunistic site 1”. In the orthosteric site, the trimethoxybenzoic acid group interacts with Trp29 from TM1 and Gln158 from TM4, both of which are in the N-domain. The central diazepane ring is cradled by a hydrophobic contact with Met33 from TM1, a previously reported determinant of the isoform specificity exhibited by dilazep and dipyridamole[42,43]. In the opportunistic site 1, the other trimethoxyphenyl ring forms pi-pi stacking interactions with Phe307 (TM7) and Phe334 (TM8), along with an H-bonding interaction with Asn338 from TM8, all of which are in the C-domain. Consistent with our structural observation, Trp29, Phe334 and Asn338 have been previously shown to affect hENT1 transport sensitivity to dilazep when mutated (Supplementary Fig. 5a)[37,44].

NBMPR binding site

NBMPR is an adenosine analog inhibitor (Fig. 3b), therefore the structure of hENT1 in complex with NBMPR could provide insights into the mechanisms of adenosine recognition by hENT1 as well as hENT1 inhibition. Deep within the central cavity of the transporter we observed a prominent F_o-F_c omit electron density peak of which the shape and size is consistent with NBMPR (Fig. 3b and Supplementary Fig. 3). The central cavity, analogous to the “orthosteric site” in the dilazep-hENT1 structure, is occupied by the adenosine-like thioinosine moiety of NBMPR. The 2’-OH and 3’-OH of the ribose moiety of NBMPR interact with the side chains of conserved Arg345 and Asp341 respectively, both of which have been previously reported to be critical for nucleoside transport activity in the ENT family member *L. donovani* LdNT2[41]. The conserved Gln158 coordinates to the N-1 and N-3 amino groups of the thioinosine moeity, suggesting this amino acid residue might be important for nucleobase recognition. Furthermore, the hydrophobic amino acids including Leu26, Met89, Leu92 and Leu442 lined by TMs 1, 2 and 11, also surround the purine moiety of NBMPR. Specifically, Leu26 and Leu442 sandwich the purine ring, bolstering the previous finding in which the mutation of Leu442Ile converts nucleoside preference to

uridine over adenosine in hENT1[37]. Met89 and Leu92 were also implicated in both purine and NBMPR binding (Supplementary Fig. 5a)[38,39]. We posit that adenosine recognition by hENT1 will be similar to the thioinosine binding by hENT1 in our structure. Therefore, hENT1 utilizes two conserved charged residues for ribose recognition, whereas nucleobase recognition is mediated by polar coordination by the conserved Gln158 in addition to hydrophobic contacts within the central cavity.

Notably, the side of the central cavity proximal to the thioinosine moiety of NBMPR is connected to a deep-hydrophobic pocket protruding into the transporter N-domain, which is lined by TM1, TM3 and TM4. In the NBMPR-hENT1 complex structure, the p-nitrobenzyl ring occupies this hydrophobic cavity (Fig. 3b). We refer to this cavity as the opportunistic site 2. Directly abutting the p-nitrobenzyl ring of NBMPR within this cavity is Gly154, and the amino acid residue at the equivalent position is serine in hENT2 and hENT3. Mutation to serine at this position in hENT1 was shown to result in a ~2,500-fold decrease in NBMPR inhibitory potency, and thus Gly154 has been suggested to be a key determinant of the isoform-specificity displayed by NBMPR[40]. Substituting glycine for serine at this position in the NBMPR-hENT1 structural model leads to narrowing the hydrophobic cavity, which would hinder the binding of the p-nitrobenzyl ring of NBMPR (Supplementary Fig. 5b), providing an explanation for the mutational effect of Gly154.

Shared and Distinct Binding Sites of Dilazep and NBMPR

Structural comparison of the NBMPR- and dilazep-bound hENT1 structures reveal that shared and distinct amino acid residues for binding these two inhibitors. In the shared orthosteric site, Gln158 appears to be important for binding the purine ring of NBMPR and the trimethoxyphenyl ring in dilazep (Fig. 4a). Because there were no previous mutagenesis studies on Gln158, we mutated Gln158 to either asparagine or serine, and found both mutations result in the abrogation of ^{3}H-NBMPR binding capacity (Fig. 4b). Structures of both transporter complexes suggest that the opportunistic site 1 is exploited for dilazep binding only, but not for NBMPR binding. To test this structural observation, we have chosen to mutate Phe307 in the opportunistic site 1, as this amino acid residue has not been previously studied. While NBMPR binding was assayed by direct binding of ^{3}H-NBMPR, dilazep binding was assayed by displacement of bound ^{3}H-NBMPR. To validate our assay, we first mutated Met33 in the orthosteric site 1 to Ile and observed a ~3-fold increase in apparent K_d for dilazep, while there is no noticeable change in K_d for NBMPR, consistent with previous mutagenesis studies concerning this specific hENT1 mutation[42,45]. We then mutated Phe307 to alanine in hENT1 and found a resulting ~90-fold increase in apparent K_d for dilazep, whereas the conservative mutation Phe307Tyr resulted in a ~4-fold decrease in apparent K_d for dilazep. However, neither Phe307Ala nor Phe307Tyr had a noticeable effect on NBMPR binding in hENT1 (Fig. 4c–d). Our functional studies confirmed the structural observation that the opportunistic site 1 contributes substantially to the binding energetics of dilazep and not NBMPR, while mutation at the shared orthosteric site disrupts NBMPR binding (due to disrupted NBMPR binding in the orthosteric site mutants, dilazep binding was not determined for Gln158Asn and Gln158Ser).

Inhibitory mechanisms of dilazep and NBMPR

The structures presented here capture hENT1 in two-inhibitor bound states, which provides insights into their inhibition mechanisms of hENT1. Based on the two-domain architecture, we reason that hENT1 will likely utilize global rocker-switch-like reorientation of N- and C-domains for the alternating-access mechanism, for its adenosine and nucleoside-analog-drug transport. These two inhibitor-bound states feature the transporter in outward-facing conformations in which the intracellular thick gate defines the outward-facing state of the transporter. In order for the transporter to transition into the inward-facing state, the extracellular thin gate is completed first upon substrate binding, followed by the extracellular thick gate formation by N- and C-domain reorientation (Fig. 5)[46]. In both inhibitor-bound hENT1 structures, dilazep and NBMPR share the orthosteric site within the central cavity of the transporter, but explore distinct opportunistic sites for inhibition of the conformational transitions of the transporter. The opportunistic site 1 for the drug dilazep is located at the region including the extracellular thin gate, and is occupied by the central diazepane ring and one of the two trimethoxyphenyl rings of the drug. Therefore, dilazep sterically prevents complete extracellular thin gate formation, which is required for the extracellular thick gate formation followed by the transition into the inward-facing state (Fig. 5). This steric blocking of extracellular gate formation has commonly been employed by competitive inhibitors in MFS and sodium-coupled neurotransmitter transporters[47–50]. In the NBMPR-bound hENT1 structure, because the opportunistic site 1 is not occupied, the extracellular thick gate formation is not sterically hindered. Notably, the p-nitrobenzyl ring of NBMPR protrudes deep into a hydrophobic cavity present within the N-domain of hENT1 (the opportunistic site 2) while the adenosine-like thioinosine group occupies the orthosteric site of the transporter. Based off of the previous studies highlighting the large conformational changes substrate-lining TMs undergo during the transport cycle[26,46,51], we speculate that TM1, TM3, and TM4 that surrounds the opportunistic site 2 are important for conformational transition, and the occupancy of this site by the p-nitrobenzyl ring of NBMPR prevents the conformational rearrangement of the N-domain required for transport (Fig. 5). To the best of our knowledge, all competitive inhibitor bound transporter structures feature steric hindrance of gate closure[47,49,50,52]. Having a competitive inhibitor blocking the transporter using an extended moiety for allosteric control of the conformational transition is unprecedented to the best of our knowledge.

Discussion

Our structural and mutagenesis studies reveal the structural basis of solute recognition and inhibition exhibited on a clinically relevant human SLC29 transporter. First, our structures uncover the molecular architecture and design principles of the SLC29 family of nucleoside transporters for the first time. Prior to this work the SLC29 family fold was hypothesized to adopt the highly conserved MFS transporter fold[2]. However, we found that the SLC29 family shows interesting differences from MFS, which follows a strict 12 TM topology. It is tempting to speculate the differences observed between the SLC29 and MFS folds could result in mechanistic differences in solute transport. Second, in combination with a wealth of previous mutagenesis studies our structures provide insights into the molecular features of nucleoside recognition and nucleoside preference exhibited by this human adenosine

transporter. Third, our structural and mutagenesis studies help us understand how the non-nucleoside vasodilator dilazep can bind and inhibit hENT1, which offers an opportunity for the rational design of improved therapeutics modulating nucleoside transport. Last, our structural analyses together with previous and current mutagenesis studies suggest that NBMPR inhibits the transporter in a unique manner, which not only provides a glimpse of the inner workings of this transporter, but also shows a previously unappreciated way to inhibit transporters of therapeutic target.

Methods

Construct screening and optimization.

The codon-optimized wild type hENT1 was synthesized in the pCEH vector with a C-terminal GFP-His_{10} tag for initial screening of transporter detergent-solution stability with fluorescence size-exclusion chromatography (FSEC)[53]. For additional screening, scale-up expression, purification and crystallization, the codon optimized wild type hENT1 cDNA was transferred to the pEG BacMam vector featuring a Precission Protease cleavable FLAG-His_{10} tagged C-terminal eGFP fusion[54]. The wild type fusion transporter exhibits monodisperse gel filtration behavior in n-dodecyl-ß-D-maltoside (DDM) detergent buffer, however the transporter loses stability upon eGFP removal and subsequent purification. To achieve a level of transporter stability amenable to biophysical studies, we used consensus mutagenesis to improve the detergent solution behavior of purified hENT1. A panel of putative stabilizing mutations and disordered loop truncations were screened for enhanced transporter detergent solution behavior. The final hENT1 construct used for crystallization (denoted as $hENT1_{cryst}$) contains the point mutations Leu168Phe, Pro175Ala, Asn288Lys and TM6–7 loop truncation Δ243–274[27], all of which were determined to enhance transporter behavior in DDM detergent.

Screening, expression and purification.

The $hENT1_{cryst}$-GFP-FLAG-His_{10} was overexpressed in HEK293S $GnTI^{-/-}$ cells by viral transduction[54]. 10 mM sodium butyrate and 10 μM dilazep were added to the virally induced cells 24 hrs post infection, and cells were harvested 72 hrs post infection. Total cell lysates containing dilazep bound fusion recombinant transporter were solubilized in 50 mM Tris-HCl (pH 8.0), 150 mM NaCl, 0.5 mM TCEP and 40 mM n-dodecyl-ß-D-maltoside (DDM) detergent for 1 hour, followed by centrifugation at 16,000rpm for 25 minutes. Detergent solubilized clarified lysate was incubated with FLAG M2 affinity resin for 1 hour, followed by resin washing with 5CV high salt buffer (20 mM Tris-HCl pH 8.0, 500 mM NaCl, 1.0 mM DDM detergent, 0.5 mM TCEP, 10 μM dilazep) followed by 5CV low salt buffer (20 mM Tris-HCl pH 8.0, 150 mM NaCl, 0.5 mM TCEP, 1.0 mM DDM detergent, 10 μM dilazep) and elution with low salt buffer supplemented with 0.2 mg/mL FLAG peptide (DYKDDDDK). Purified $hENT1_{cryst}$ fusion was then concentrated to 0.75 mg/mL and treated with 1:10 Precission Protease and 1:10 EndoH for 2 hours, to simultaneously cleave the GFP-FLAG-His_{10} tag and remove N-linked glycan. The deglycosylated, free transporter was then further purified with size-exclusion chromatography (Superdex 200) in 20 mM Tris-HCl pH 8.0, 150 mM NaCl, 0.5 mM DDM, 0.5 mM TCEP and 10 μM dilazep. For crystallization with NBMPR, protein expression and purification was consistent with the

dilazep condition, except expression was performed apo and NBMPR was incorporated at all stages of the preparation (10 μM during extraction and anti-FLAG purification, 1.0 μM during gel filtration). For proteoliposome reconstitution, protein was prepared apo, and 5.0 mM n-decyl-ß-D-maltoside (DM) detergent was used in the final gel filtration step.

Crystallization.

Inhibitor bound $hENT1_{cryst}$ was crystallized with the lipidic cubic phase method[55]. Purified inhibitor-bound protein was concentrated to 40 mg ml^{-1} prior to mixing with monoolein (Sigma) in a 40:60 weight-weight ratio. Crystallization was facilitated at room temperature in 96 well glass sandwich plates (MiTeGen) with 150 nL mesophase and 1.0 μL crystallization solution. The crystallization condition yielding the best diffracting crystals of the dilazep bound $hENT1_{cryst}$ consisted of 35–50% PEG 400, 0.1M glycine pH 9.0 and 0.5 M NaCl. Plate-like crystals appeared 12 hours after setting up trays, and reached a full size of 50×20 μm in 3–5 days. Wells were opened with a tungsten-carbide glass cutter (MiTeGen), and crystals were harvested with 75 um MiTeGen micromounts and directly cooled in LN_2. Dilazep-transporter crystals were used for the heavy-atom soaks for phasing, and soaks were carried out as described previously[56]. For all heavy-atom screens, soaks were carried out for 24 hours prior to well re-opening and harvesting. For the NBMPR bound $hENT1_{cryst}$ structure, the crystal was obtained from 30% PEG 500 MME, 0.1M magnesium chloride hexahydrate and 0.1M Tris-HCl pH 8.0. The crystal grew to full size after 7 days.

Structure determination.

All data was collected on the NE-CAT remote access 24ID-C and 24ID-E beamlines at the Advanced Photon Source at a wavelength of 0.979 Å. The native data for the dilazep structure was processed with Mosflm and the derivative data was processed with the NE-CAT RAPD pipeline[57]. A 90-degree wedge of a single $hENT1_{cryst}$ dilazep crystal yielded a complete dataset, with X-rays diffracting beyond 2.1 Å in the best direction, with and a space group of $P3_221$. Due to mild diffraction anisotropy, anisotropic truncation was performed with the STARANISO server. Of the initial heavy-atom derivatives screened, K_2PtCl_4 soaks yielded crystals that were highly isomorphous to the native crystal and diffracted X-rays beyond 3.0 Å resolution. Full 360-degree datasets were collected on 3 separate isomorphous K_2PtCl_4 soaked crystals, and these datasets were combined to increase anomalous multiplicity. Phasing was performed using high-resolution native data and merged derivative data with single-isomorphous replacement with anomalous scattering (SIRAS). Platinum sites were determined with the SHELXC/D/E software suite[58], followed by phasing and extreme density modification to 5.0 Å with AutoSol in the Phenix software suite[59] yielding a figure of merit (FOM) of 0.50. An initial partial model was built by placing 11 idealized alpha-helices into the asymmetric unit of this experimental map, with unambiguous helix connectivity apparent for TMDs 2–6. An experimental SIRAS map phase-extended with extreme density modification to 3.5 Å (FOM of 0.33) was then utilized to confirm helix direction, and to perform manual adjustments of the initial model. Combined phases were then determined from this initial model and anomalous dispersion from the merged platinum data (MR-SAD) to 3.5 Å and extended to 2.9 Å with density modification. The transporter was registered and side-chains were built for roughly 80% of

the molecule using the resulting MR-SAD map. This working model was then transferred to the highest resolution native data with molecular replacement, and iterative cycles of building and refinement in Phenix were performed. The final model is of good quality with a Phenix reported R_{work}/R_{free}= 0.20/0.24 and excellent Ramachandran statistics (98.7% favored, 1.3% allowed, no outliers), containing hENT1 residues 7–452 (hENT1 residues 1–6, 49–73, 241–280, 453–456, missing).

For the NBMPR bound $hENT1_{cryst}$ structure, a 110-degree wedge of a single crystal yielded a complete dataset and was processed with XDS[60], with X-rays diffracting beyond 3.0 Å. Due to moderate diffraction anisotropy, anisotropic truncation was performed with the STARANISO server. Intensity statistics indicated merohedral twinning with the apparent space group P622 and the actual space group $P6_1$ with the twin operator of h, -h-k, -l. The protein portion of the final dilazep bound transporter structure was used as a search model for molecular replacement, resulting in the placement of two transporter molecules per asymmetric unit. Refinements were carried out against the anisotropically corrected X-ray data to a 2.9 Å, using an intensity-based twin refinement in Phenix[59] and Refmac5[61]. Free-R flags were written in the highest possible point group of the lattice, and subsequently expanded to the final space group of $P6_1$ to prevent cross-contamination between the working and free set during the twinned refinements. Multiple rounds of model building and refinement resulted in a Phenix reported R_{work}/R_{free}=0.21/0.25. The final model exhibits good protein geometry (95.9% Ramachandran favored, 4.1% allowed, no outliers) and a clashscore of 3.4.

Inhibitor binding assays.

Scintillation proximity assays (SPAs) were performed using anti-FLAG M2 purified hENT1-GFP-FLAG-His_{10} fusion transporter and Cu-PVT beads in 20 mM Tris-HCl, 150 mM NaCl, 1.0 mM DDM, 0.5 mg/mL BSA in a total volume of 0.5 mL. For saturation binding of ^{3}H-NBMPR (5.5 Ci/mmol, Moravek Inc.) to wild type and $hENT1_{cryst}$ fusion constructs (Fig. 1a), radiochemical was successively titrated onto 10 nM transporter immobilized to 4.0 mg/mL Cu-PVT beads, with scintillation counting following each addition. For saturation binding of ^{3}H-NBMPR to $hENT1_{cryst}$ and mutants in the $hENT1_{cryst}$ background (Fig. 4b), radiochemical was successively titrated onto 6.25 nM transporter immobilized to 3.0 mg/mL Cu-PVT beads. K_d was determined in GraphPad Prism, using a non-linear regression equation accounting for ligand depletion. For cold competition assays, unlabeled dilazep was titrated onto SPA mixture containing 85 nM fusion transporter, 100 nM ^{3}H-NBMPR and 3.0 mg/mL Cu-PVT beads. Apparent dilazep-displacement K_d were determined from fitting the data in GraphPad Prism to a non-linear regression equation to describe competitive binding accounting for ligand depletion.

Transport assays.

Nucleoside transport assays were performed in a counterflow manner, using purified hENT1 reconstituted into proteoliposomes. Protein purified in 5 mM DM was reconstituted using 10 mg ml^{-1} of 1-palmitoyl-2-oleoyl-sn-glycero-3-phosphoethanolamine (POPE) and 1-palmitoyl-2-oleoyl-sn-glycero-3-phospho-(1'-rac-glycerol) (POPG) in a 3:1 ratio in the presence of transport buffer (20 mM HEPES pH 7.4, 150 mM NaCl) as described

previously[62] with the following adjustment: DM detergent was removed with 4 × 10 hour treatment with 100 mg ml^{-1} BioBeads (BioRad). Reconstituted proteoliposomes were loaded with 1.0 mM cold uridine via five cycles of LiN_2 freeze thaw, followed by extrusion through the Avanti Mini-Extruder loaded with a 1.0 μM filter. Extraliposomal cold nucleoside was removed from the loaded vesicles with illustra MicroSpin G-50 columns (GE Healthcare), and the transport reaction was immediately initiated by 1:50 dilution of the proteoliposomes (v/v) into 500 uL transport buffer containing 0.2 μM ^{3}H-uridine (17 Ci/mmol, Moravek). Reactions were terminated after 90 seconds by rapid filtration of the assay mixture over a 1.0 μM GF/B glass microfibre filter (Whatman), followed by rapid washing with 4 × 2.0 mL transport buffer (performed on a 96-well Brandel harvester). Filters were then added to 5.0 mL liquid scintillation counting fluid and analyzed by scintillation counting after 12 hours.

Reporting Summary statement.

Further information on experimental design is available in the Nature Research Reporting Summary linked to this article.

Data Availability statement.

Atomic coordinates and structure factors for the reported crystal structures are deposited in the Protein Data Bank under accession codes 6OB6 (hENT1 in complex with NBPMR) and 6OB7 (hENT1 in complex with dilazep). Source data for Figure 1a, 4b–d and Supplementary Figure 1 are available with the paper online. Any other data pertaining to this paper is available upon request. Correspondence and requests for materials should be addressed to S.-Y.L. (seok-yong.lee@duke.edu).

Supplementary Material

Refer to Web version on PubMed Central for supplementary material.

Acknowledgements

Data were collected at beamlines 24-ID-C and 22-ID in the Advanced Photon Source. We thank A. Kuk for help with X-ray crystallography and critical manuscript reading and Y. Ying for help with membrane protein biochemistry. This work was supported by NIH R35 NS097241 (S.-Y.L.). Beamline 24-ID-C is funded by P41GM103403 and S10 RR029205.

Main-text References

1. Young JD, Yao SYM, Sun L, Cass CE & Baldwin SA Human equilibrative nucleoside transporter (ENT) family of nucleoside and nucleobase transporter proteins. Xenobiotica 38, 995–1021, doi: 10.1080/00498250801927427 (2008). [PubMed: 18668437]
2. Boswell-Casteel RC & Hays FA Equilibrative nucleoside transporters—A review. Nucleosides, Nucleotides and Nucleic Acids 36, 7–30, doi:10.1080/15257770.2016.1210805 (2017).
3. Griffiths M et al. Cloning of a human nucleoside transporter implicated in the cellular uptake of adenosine and chemotherapeutic drugs. Nat. Med 3, 89–93 (1997). [PubMed: 8986748]
4. Molina-Arcas M, Casado FJ & Pastor-Anglada M Nucleoside transporter proteins. Curr Vasc Pharmacol 7, 426–434, doi:CVP-Abs-054 [pii] (2009). [PubMed: 19485885]
5. Borea PA, Gessi S, Merighi S & Varani K Adenosine as a Multi-Signalling Guardian Angel in Human Diseases: When, Where and How Does it Exert its Protective Effects? Trends in

Pharmacological Sciences 37, 419–434, doi:10.1016/j.tips.2016.02.006 (2016). [PubMed: 26944097]

6. Mubagwa K & Flameng W Adenosine, adenosine receptors and myocardial protection: an updated overview. Cardiovasc. Res 52, 25–39 (2001). [PubMed: 11557231]
7. Choi DS et al. The type 1 equilibrative nucleoside transporter regulates ethanol intoxication and preference. Nat Neurosci 7, 855–861, doi:10.1038/nn1288 (2004). [PubMed: 15258586]
8. Baldwin SA, Mackey JR, Cass CE & Young JD Nucleoside transporters: molecular biology and implications for therapeutic development. Mol Med Today 5, 216–224, doi:10.1016/S1357-4310(99)01459-8 (1999). [PubMed: 10322314]
9. Young JD, Yao SY, Baldwin JM, Cass CE & Baldwin SA The human concentrative and equilibrative nucleoside transporter families, SLC28 and SLC29. Mol Aspects Med 34, 529–547, doi:10.1016/j.mam.2012.05.007 (2013). [PubMed: 23506887]
10. Yoshida H et al. Effects of an anti-platelet drug (dilazep) in IgA nephropathy: comparison of clinical effects with renal biopsy findings. Nihon Jinzo Gakkai Shi 36, 339–344 (1994). [PubMed: 8022106]
11. Fitzgerald G Drug Therapy: Dipyridamole. The New England Journal of Medicine 316, 1247–1257 (1987). [PubMed: 3553945]
12. Guo Z et al. Rapamycin-inspired macrocycles with new target specificity. Nat Chem, doi:10.1038/s41557-018-0187-4 (2018).
13. Buolamwini J Nucleoside transport inhibitors: structure activity relationships and potential therapeutic applications. Current Medicinal Chemistry 4, 35–66 (1996).
14. Lin W & Buolamwini JK Synthesis, flow cytometric evaluation, and identification of highly potent dipyridamole analogues as equilibrative nucleoside transporter 1 inhibitors. J Med Chem 50, 3906–3920, doi:10.1021/jm070311l (2007). [PubMed: 17636949]
15. Gupte A & Buolamwini JK CoMFA and CoMSIA 3D-QSAR studies on S6-(4-nitrobenzyl)mercaptopurine riboside (NBMPR) analogs as inhibitors of human equilibrative nucleoside transporter 1 (hENT1). Bioorganic & Medicinal Chemistry Letters 19, 314–318, doi:10.1016/j.bmcl.2008.11.092 (2009). [PubMed: 19091561]
16. Farrell JJ et al. Human Equilibrative Nucleoside Transporter 1 Levels Predict Response to Gemcitabine in Patients With Pancreatic Cancer. Gastroenterology 136, 187–195, doi:10.1053/j.gastro.2008.09.067 (2009). [PubMed: 18992248]
17. Greenhalf W et al. Pancreatic Cancer hENT1 Expression and Survival From Gemcitabine in Patients From the ESPAC-3 Trial. JNCI: Journal of the National Cancer Institute 106, doi:10.1093/jnci/djt347 (2014).
18. Hagmann W, Jesnowski R & Löhr JM Interdependence of gemcitabine treatment, transporter expression, and resistance in human pancreatic carcinoma cells. Neoplasia 12, 740–747 (2010). [PubMed: 20824050]
19. Marcé S et al. Expression of human equilibrative nucleoside transporter 1 (hENT1) and its correlation with gemcitabine uptake and cytotoxicity in mantle cell lymphoma. Haematologica 91, 895–902 (2006). [PubMed: 16818276]
20. Marechal R et al. Human equilibrative nucleoside transporter 1 and human concentrative nucleoside transporter 3 predict survival after adjuvant gemcitabine therapy in resected pancreatic adenocarcinoma. Clin Cancer Res 15, 2913–2919, doi:10.1158/1078-0432.CCR-08-2080 (2009). [PubMed: 19318496]
21. Spratlin J et al. The absence of human equilibrative nucleoside transporter 1 is associated with reduced survival in patients with gemcitabine-treated pancreas adenocarcinoma. Clin Cancer Res 10, 6956–6961, doi:10.1158/1078-0432.CCR-04-0224 (2004). [PubMed: 15501974]
22. Tanaka M et al. Gemcitabine metabolic and transporter gene polymorphisms are associated with drug toxicity and efficacy in patients with locally advanced pancreatic cancer. Cancer 116, 5325–5335, doi:10.1002/cncr.25282 (2010). [PubMed: 20665488]
23. Voutsadakis IA Molecular predictors of gemcitabine response in pancreatic cancer. World J Gastrointest Oncol 3, 153–164, doi:10.4251/wjgo.v3.i11.153 (2011). [PubMed: 22110842]

24. Johnson ZL, Cheong CG & Lee SY Crystal structure of a concentrative nucleoside transporter from Vibrio cholerae at 2.4 A. Nature 483, 489–493, doi:10.1038/nature10882 (2012). [PubMed: 22407322]
25. Johnson ZL et al. Structural basis of nucleoside and nucleoside drug selectivity by concentrative nucleoside transporters. Elife 3, e03604, doi:10.7554/eLife.03604 (2014). [PubMed: 25082345]
26. Hirschi M, Johnson ZL & Lee S-Y Visualizing multistep elevator-like transitions of a nucleoside transporter. Nature 545, 66–70, doi:10.1038/nature22057 (2017). [PubMed: 28424521]
27. Aseervatham J, Tran L, Machaca K & Boudker O The Role of Flexible Loops in Folding, Trafficking and Activity of Equilibrative Nucleoside Transporters. PloS One 10, e0136779, doi:10.1371/journal.pone.0136779 (2015). [PubMed: 26406980]
28. Huang W, Zeng X, Shi Y & Liu M Functional characterization of human equilibrative nucleoside transporter 1. Protein Cell 8, 284–295, doi:10.1007/s13238-016-0350-x (2017). [PubMed: 27995448]
29. Sundaram M et al. Topology of a Human Equilibrative, Nitrobenzylthioinosine (NBMPR)-sensitive Nucleoside Transporter (hENT1) Implicated in the Cellular Uptake of Adenosine and Anti-cancer Drugs. Journal of Biological Chemistry 276, 45270–45275, doi:10.1074/jbc.M107169200 (2001). [PubMed: 11584005]
30. Deng D et al. Molecular basis of ligand recognition and transport by glucose transporters. Nature 526, 391–396, doi:10.1038/nature14655 (2015). [PubMed: 26176916]
31. Abramson J et al. Structure and mechanism of the lactose permease of Escherichia coli. Science 301, 610–615, doi:10.1126/science.1088196 (2003). [PubMed: 12893935]
32. Jarvis SM, McBride D & Young JD Erythrocyte nucleoside transport: asymmetrical binding of nitrobenzylthioinosine to nucleoside permeation sites. J Physiol 324, 31–46 (1982). [PubMed: 7097603]
33. Jarvis SM & Young JD Nucleoside transport in rat erythrocytes: two components with differences in sensitivity to inhibition by nitrobenzylthioinosine and p-chloromercuriphenyl sulfonate. J Membr Biol 93, 1–10 (1986). [PubMed: 3025447]
34. Agbanyo FR, Cass CE & Paterson AR External location of sites on pig erythrocyte membranes that bind nitrobenzylthioinosine. Mol Pharmacol 33, 332–337 (1988). [PubMed: 3352596]
35. Yao SYM, Ng AML, Cass CE & Young JD Role of cysteine 416 in N-ethylmaleimide sensitivity of human equilibrative nucleoside transporter 1 (hENT1). Biochem J 475, 3293–3309, doi:10.1042/BCJ20180543 (2018). [PubMed: 30254099]
36. Zhang XC, Zhao Y, Heng J & Jiang D Energy coupling mechanisms of MFS transporters. Protein Sci 24, 1560–1579, doi:10.1002/pro.2759 (2015). [PubMed: 26234418]
37. Paproski Robert J. et al. Mutation of Trp 29 of human equilibrative nucleoside transporter 1 alters affinity for coronary vasodilator drugs and nucleoside selectivity. Biochemical Journal 414, 291–300, doi:10.1042/BJ20080074 (2008). [PubMed: 18462193]
38. Endres CJ & Unadkat JD Residues Met89 and Ser160 in the human equilibrative nucleoside transporter 1 affect its affinity for adenosine, guanosine, S6-(4-nitrobenzyl)-mercaptopurine riboside, and dipyridamole. Mol Pharmacol 67, 837–844, doi:10.1124/mol.104.008102 (2005). [PubMed: 15557207]
39. Endres CJ, Sengupta DJ & Unadkat JD Mutation of leucine-92 selectively reduces the apparent affinity of inosine, guanosine, NBMPR [S6-(4-nitrobenzyl)-mercaptopurine riboside] and dilazep for the human equilibrative nucleoside transporter, hENT1. Biochemical Journal 380, 131–137, doi:10.1042/bj20031880 (2004). [PubMed: 14759222]
40. SenGupta DJ & Unadkat JD Glycine 154 of the equilibrative nucleoside transporter, hENT1, is important for nucleoside transport and for conferring sensitivity to the inhibitors nitrobenzylthioinosine, dipyridamole, and dilazep. Biochemical Pharmacology 67, 453–458, doi:10.1016/j.bcp.2003.09.018 (2004). [PubMed: 15037197]
41. Arastu-Kapur S, Ford E, Ullman B & Carter NS Functional analysis of an inosine-guanosine transporter from Leishmania donovani. The role of conserved residues, aspartate 389 and arginine 393. J Biol Chem 278, 33327–33333, doi:10.1074/jbc.M305141200 (2003). [PubMed: 12807872]

42. Visser F et al. Mutation of Residue 33 of Human Equilibrative Nucleoside Transporters 1 and 2 Alters Sensitivity to Inhibition of Transport by Dilazep and Dipyridamole. Journal of Biological Chemistry 277, 395–401, doi:10.1074/jbc.M105324200 (2002). [PubMed: 11689555]
43. Visser F, Baldwin SA, Isaac RE, Young JD & Cass CE Identification and Mutational Analysis of Amino Acid Residues Involved in Dipyridamole Interactions with Human and Caenorhabditis elegans Equilibrative Nucleoside Transporters. Journal of Biological Chemistry 280, 11025–11034, doi:10.1074/jbc.M410348200 (2005). [PubMed: 15649894]
44. Visser F et al. Residues 334 and 338 in Transmembrane Segment 8 of Human Equilibrative Nucleoside Transporter 1 Are Important Determinants of Inhibitor Sensitivity, Protein Folding, and Catalytic Turnover. Journal of Biological Chemistry 282, 14148–14157, doi:10.1074/jbc.M701735200 (2007). [PubMed: 17379602]
45. Visser F et al. Residue 33 of human equilibrative nucleoside transporter 2 is a functionally important component of both the dipyridamole and nucleoside binding sites. Mol Pharmacol 67, 1291–1298, doi:10.1124/mol.104.005884 (2005). [PubMed: 15644498]
46. Quistgaard EM, Löw C, Guettou F & Nordlund P Understanding transport by the major facilitator superfamily (MFS): structures pave the way. Nat. Rev. Mol. Cell Biol. 17, 123–132, doi:10.1038/nrm.2015.25 (2016). [PubMed: 26758938]
47. Deng D et al. Crystal structure of the human glucose transporter GLUT1. Nature 510, 121–125, doi:10.1038/nature13306 (2014). [PubMed: 24847886]
48. Krishnamurthy H & Gouaux E X-ray structures of LeuT in substrate-free outward-open and apo inward-open states. Nature 481, 469–474, doi:10.1038/nature10737 (2012). [PubMed: 22230955]
49. Penmatsa A, Wang KH & Gouaux E X-ray structure of dopamine transporter elucidates antidepressant mechanism. Nature 503, 85–90, doi:10.1038/nature12533 (2013). [PubMed: 24037379]
50. Coleman JA, Green EM & Gouaux E X-ray structures and mechanism of the human serotonin transporter. Nature 532, 334–339, doi:10.1038/nature17629 (2016). [PubMed: 27049939]
51. Nomura N et al. Structure and mechanism of the mammalian fructose transporter GLUT5. Nature 526, 397–401, doi:10.1038/nature14909 (2015). [PubMed: 26416735]
52. Singh SK, Piscitelli CL, Yamashita A & Gouaux E A competitive inhibitor traps LeuT in an open-to-out conformation. Science 322, 1655–1661, doi:10.1126/science.1166777 (2008). [PubMed: 19074341]

Methods only references

53. Kawate T & Gouaux E Fluorescence-detection size-exclusion chromatography for precrystallization screening of integral membrane proteins. Structure 14, 673–681, doi:10.1016/j.str.2006.01.013 (2006). [PubMed: 16615909]
54. Goehring A et al. Screening and large-scale expression of membrane proteins in mammalian cells for structural studies. Nat Protoc 9, 2574–2585, doi:10.1038/nprot.2014.173 (2014). [PubMed: 25299155]
55. Landau EM & Rosenbusch JP Lipidic cubic phases: A novel concept for the crystallization of membrane proteins. Proceedings of the National Academy of Sciences 93, 14532–14535, doi:10.1073/pnas.93.25.14532 (1996).
56. Li D, Pye VE & Caffrey M Experimental phasing for structure determination using membrane-protein crystals grown by the lipid cubic phase method. Acta Crystallogr D Biol Crystallogr 71, 104–122, doi:10.1107/S1399004714010360 (2015). [PubMed: 25615865]
57. Battye TG, Kontogiannis L, Johnson O, Powell HR & Leslie AG iMOSFLM: a new graphical interface for diffraction-image processing with MOSFLM. Acta Crystallogr D Biol Crystallogr 67, 271–281, doi:10.1107/S0907444910048675 (2011). [PubMed: 21460445]
58. Schneider TR & Sheldrick GM Substructure solution with SHELXD. Acta Crystallogr D Biol Crystallogr 58, 1772–1779 (2002). [PubMed: 12351820]
59. Adams PD et al. PHENIX: a comprehensive Python-based system for macromolecular structure solution. Acta Crystallogr D Biol Crystallogr 66, 213–221, doi:10.1107/S0907444909052925 (2010). [PubMed: 20124702]

60. Kabsch W Xds. Acta Crystallogr D Biol Crystallogr 66, 125–132, doi:10.1107/S0907444909047337 (2010). [PubMed: 20124692]

61. Murshudov GN et al. REFMAC5 for the refinement of macromolecular crystal structures. Acta Crystallogr D Biol Crystallogr 67, 355–367, doi:10.1107/S0907444911001314 (2011). [PubMed: 21460454]

62. Johnson ZL & Lee SY Liposome reconstitution and transport assay for recombinant transporters. Methods Enzymol 556, 373–383, doi:10.1016/bs.mie.2014.11.048 (2015). [PubMed: 25857791]

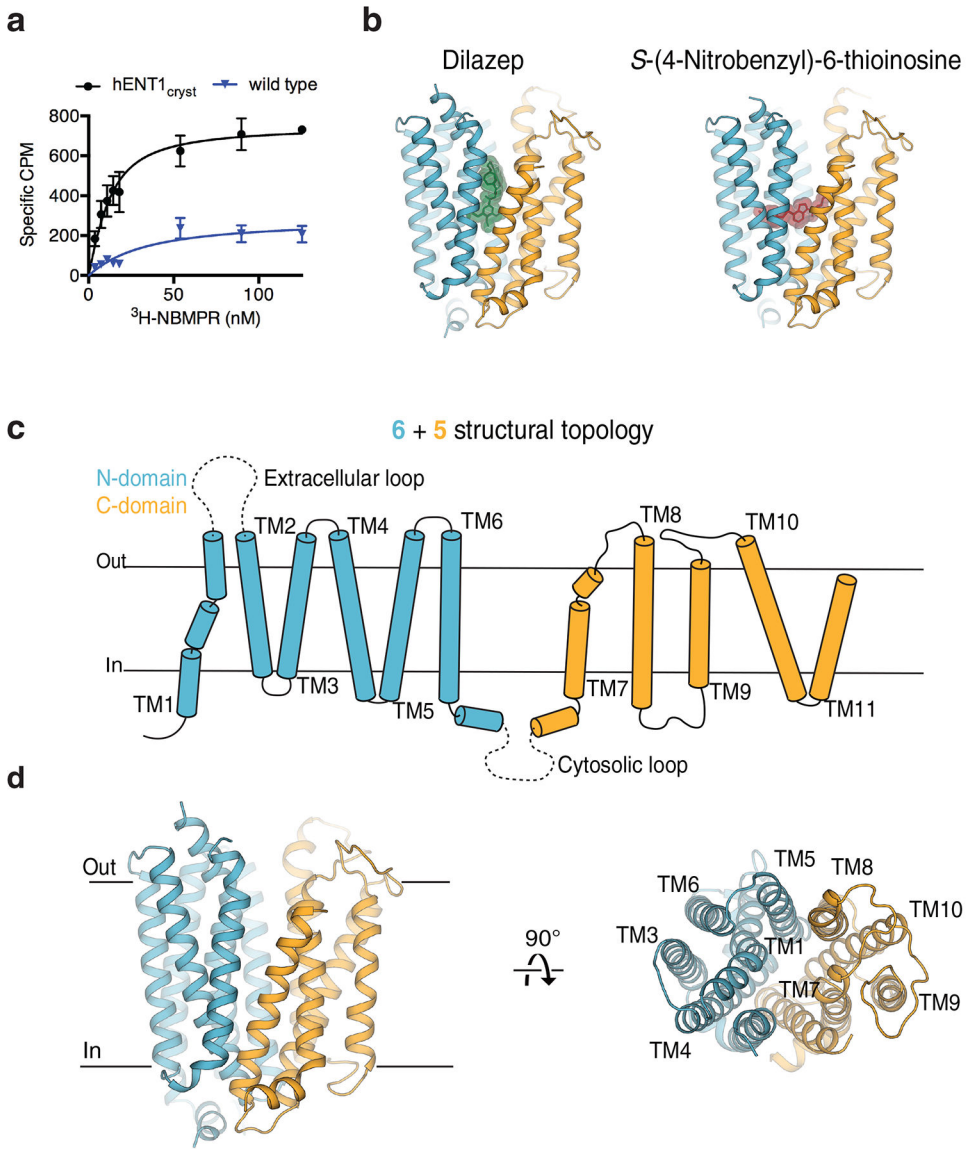

Figure 1 |. Crystal structures of human ENT1$_{cryst}$.

a, Saturation binding of the wild type hENT1 (blue triangles) and hENT1$_{cryst}$ constructs (black circles) to the hENT1-specific AdoRI ^{3}H-NBMPR (Experiments were performed in biological triplicate of technical duplicates, with error bars representing ± S.E.M.) **b**, Dilazep bound (left) and NBMPR bound (right) transporter crystal structures, with ligands highlighted and depicted as sticks. **c**, Diagram of hENT1$_{cryst}$ membrane topology **d**, Overall protein fold of the *de novo* phased, high resolution dilazep bound transporter structure, viewed from the membrane plane (left) and extracellular side (right).

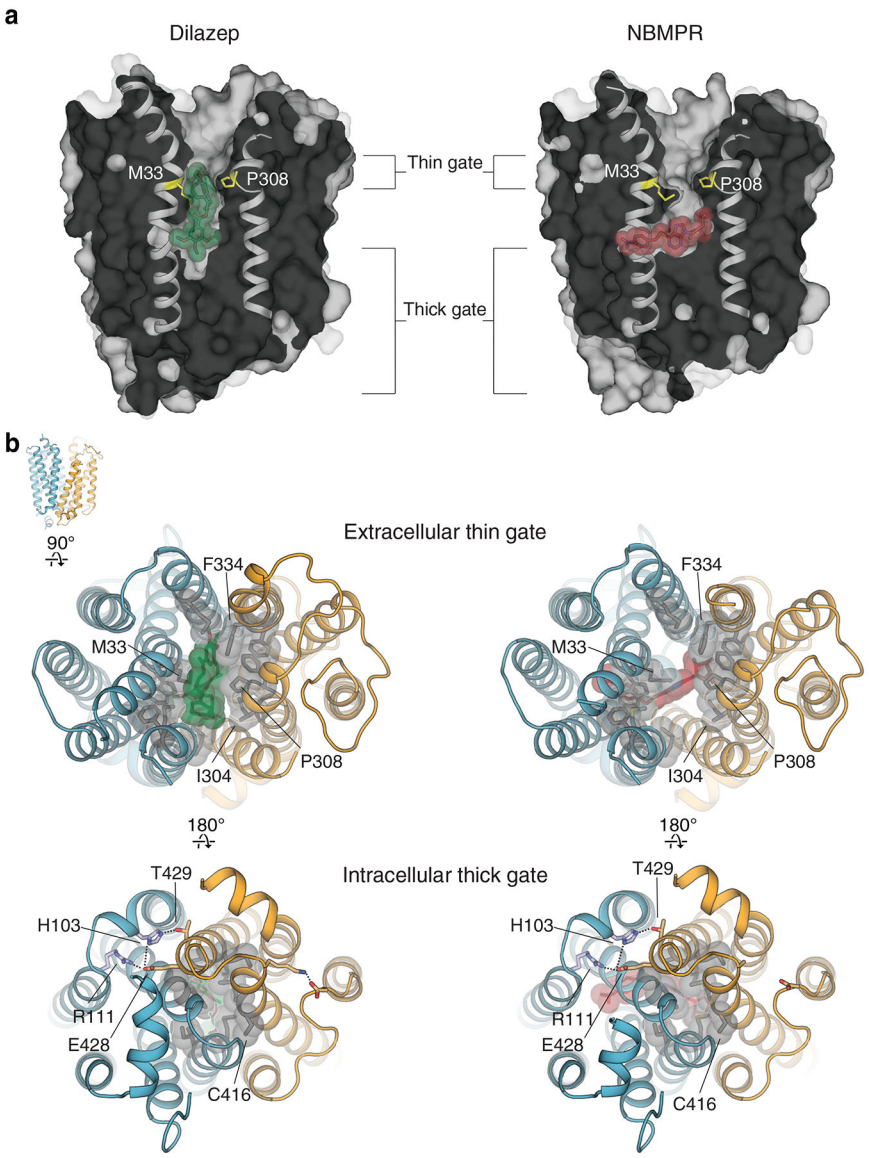

Figure 2 |. hENT1$_{cryst}$ structures capture the outward-facing state.

a, Dilazep and NBMPR bound human ENT$_{cryst}$ adopt outward-facing conformations. **b**, The extracellular thin gate cradles part of dilazep (top left), whereas NBMPR does not physically contact the thin gate (top right). The thick gate (bottom) tightly seals the central cavity from the intracellular side in both inhibitor bound structures. Hydrophobic residues highlighted in grey, with polar and charged residues shown as sticks.

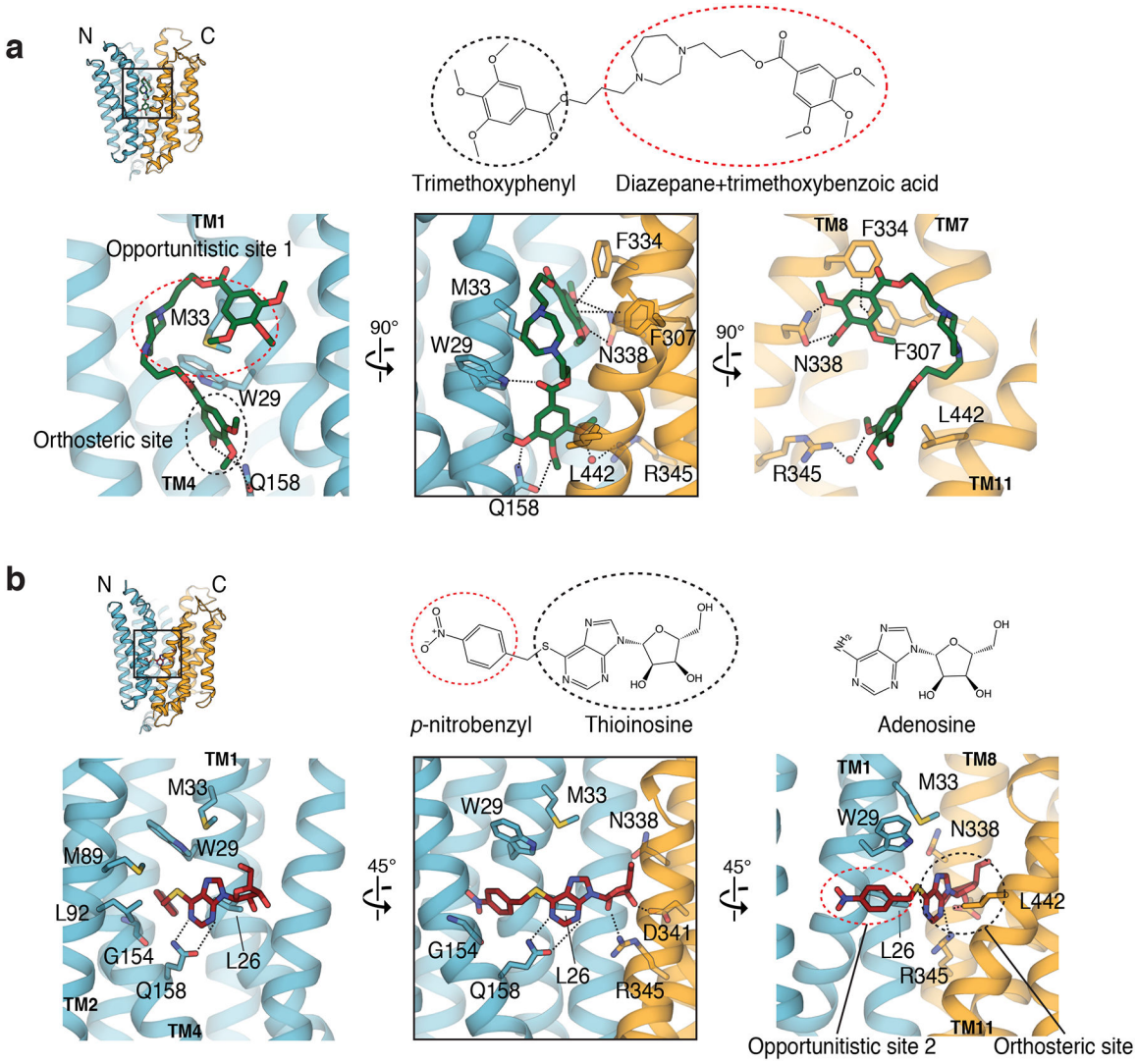

Figure 3 |. Adenosine reuptake inhibitor binding sites.

a, Dilazep binding site with residues participating in transporter-inhibitor interactions depicted as sticks. **b**, NBMPR binding site with residues in proximity to the inhibitor depicted as sticks. TM2 and TM11 omitted for clarity in central panel.

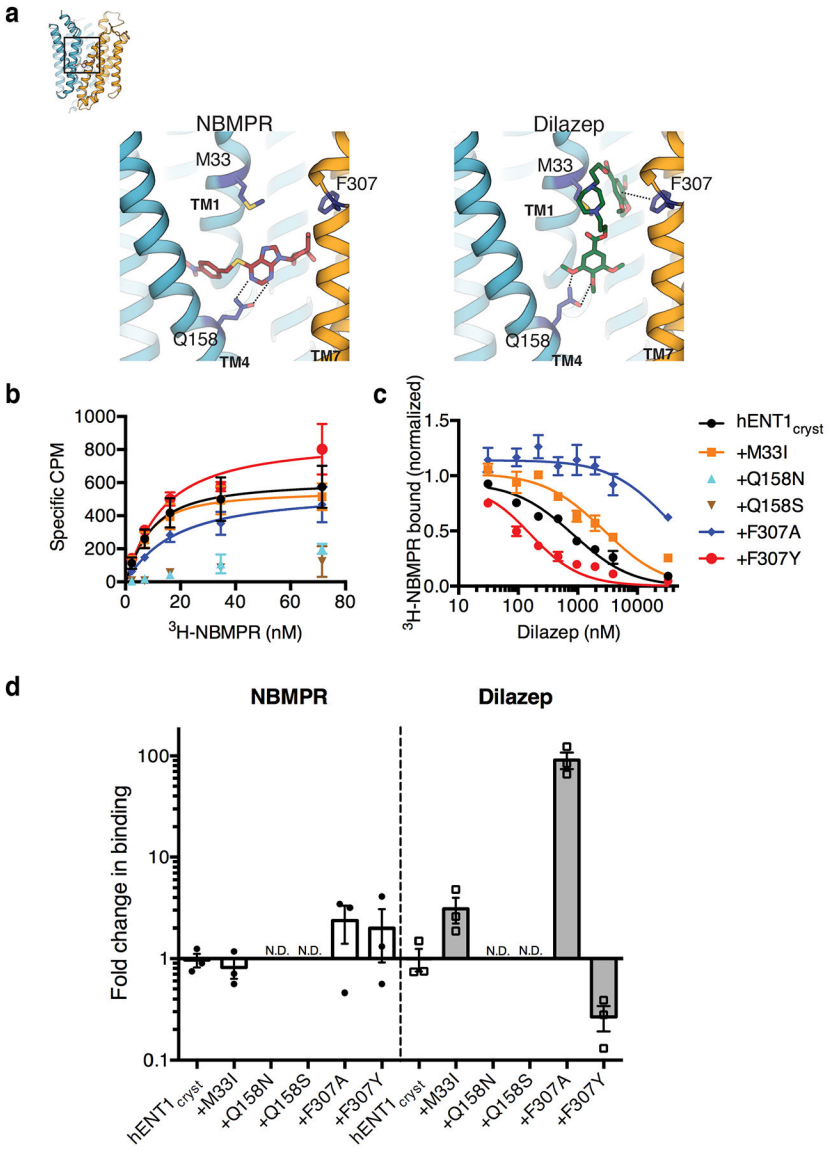

Figure 4 |. NBMPR and dilazep explore shared and distinct binding sites.

a, NBMPR and dilazep binding sites, with key interacting residues depicted as sticks. **b**, Saturation binding of ^{3}H-NBMPR and **c**, cold dilazep displacement of ^{3}H-NBMPR from hENT1$_{cryst}$ and mutants in the hENT1$_{cryst}$ background (experiments performed in biological triplicate of technical duplicates, with error bars representing ± S.E.M). Weak to no ^{3}H-NBMPR binding was determined for Q158N and Q158S within these assay conditions. **d**, Relative fold change in determined ^{3}H-NBMPR K_d and cold dilazep displacement K_d values upon introduction of mutations into the hENT1$_{cryst}$ background (individual K_d values from each biological replicate compared to the average hENT1$_{cryst}$ K_d value, with error bars representing ± S.E.M). Due to weak ^{3}H-NBMPR binding within the assay for Q158N and Q158S, relative fold changes in binding not determined.

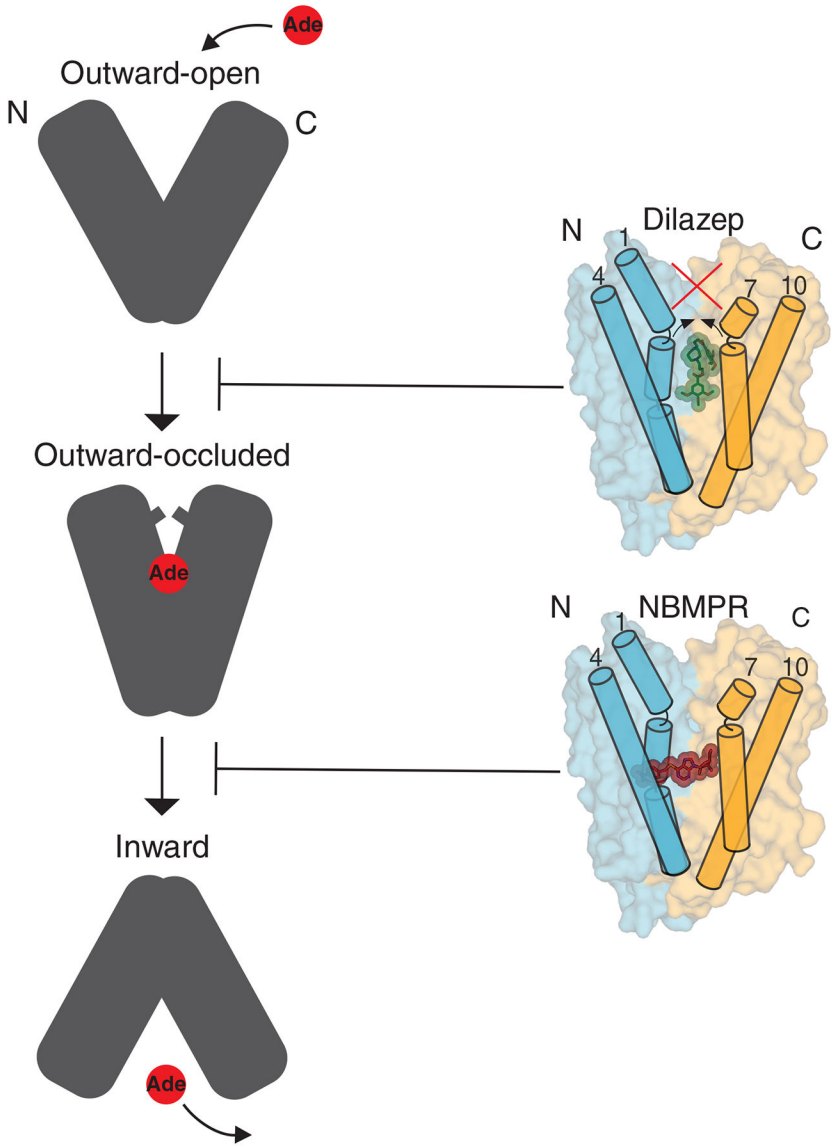

Figure 5 |. Inhibitory mechanisms.

Hypothetical mechanisms of inhibition exhibited by dilazep and NBMPR. Transport inhibition mediated by dilazep involves steric block of extracellular gate occlusion, preventing the outward-open to outward-occluded transition in the transport cycle. The nitrobenzene moiety of NBMPR occupies a deep hydrophobic pocket lined by TMs 1, 3 and 4, possibly preventing rearrangement of the N-domain required for conformational transition during the transport cycle.

Table 1

Data collection, phasing and refinement statistics

	Dilazep, Native[b,d] (PDB 6OB7)	Dilazep, Pt Derivative[c]	NBMPR, Native[b,d] (PDB 6OB6)
Data collection			
Space group	P 3_2 2 1	P 3_2 2 1	P 6_1
Cell dimensions			
a, *b*, *c* (Å)	72.0 72.0 173.4	72.2 72.2 172.3	72.5 72.5 335.7
α, *β*, *γ* (°)	90 90 120	90 90 120	90 90 120
Resolution (Å)	62.39–2.30 (2.38–2.30)[a]	62.53–2.90 (3.08–2.90)	62.82–2.90 (3.08–2.90)
R_{pim}	0.11 (0.56)	0.07 (0.40)	0.34 (1.98)
$I/\sigma(I)$	6.0 (1.4)	8.7 (2.2)	4.0 (0.8)
$CC_{1/2}$	0.99 (0.39)	0.99 (0.77)	0.93 (0.33)
Completeness (%)	91.8 (82.4)	100.0 (100.0)	74.9 (19.3)
Redundancy	4.6 (4.1)	56.5 (49.8)	7.8 (8.0)
Refinement			
Resolution (Å)	62.39–2.30 (2.38–2.30)		62.82–2.90 (3.08–2.90)
No. reflections	21962 (1924)		16459 (442)
R_{work} / R_{free}	0.20/0.24		0.21/0.25[e]
No. atoms			
Protein	5953		10,934
Ligand	602		92
Water	63		0
B factors			
Protein	24.0		29.2
Ligand/ion	39.7		30.5
Water	24.6		n/a
R.m.s deviations			
Bond lengths (Å)	0.005		0.004
Bond angles (°)	1.0		0.9

[a] Values in parentheses are for highest-resolution shell.

[b] X-ray data from a single crystal.

[c] X-ray data from 3 crystals.

[d] X-ray data anisotropically corrected with the Staraniso webserver.

[e] Phenix reported R-factors from twin-corrected structure factors (twin operator h, -h-k, -l).